

Article

The Effect of B on the Co-Segregation of C-Cr at Grain Boundaries in Austenitic Steels

Xin Yan ¹, Panpan Xu ^{2,*}, Peide Han ^{1,*}, Nan Dong ¹ , Jian Wang ¹  and Caili Zhang ¹¹ College of Materials Science and Engineering, Taiyuan University of Technology, Taiyuan 030024, China² College of Physics and Electronic Information, Weifang University, Weifang 261061, China

* Correspondence: xupan0122@163.com (P.X.); hanpeide@tyut.edu.cn (P.H.)

Abstract: In austenitic steels, the co-segregation of C and Cr at grain boundaries can result in the formation of Cr₂₃C₆. However, the addition of B to steels can effectively reduce the amount of Cr₂₃C₆ formed and inhibit its ripening in experiments, simultaneously transforming it into Cr₂₃(BC)₆. Therefore, the effect of B on the co-segregation of C and Cr at the Σ5(210), Σ9(221) and Σ11(113) grain boundaries in austenitic steels was investigated using density functional theory. The results indicate that B, C, and Cr all tend to segregate at the three grain boundaries, with B and C showing a stronger segregation tendency. Furthermore, co-segregation of C and Cr with short distances occurs readily at the Σ5(210), Σ9(221) and Σ11(113) grain boundaries. The presence of B at grain boundaries can impede the segregation of Cr, particularly at the Σ9(221) and Σ11(113) grain boundaries. When B is pre-segregating at the Σ5(210) grain boundary, B, C, and Cr tend to co-segregate at the grain boundary. The grain boundary B hinders the accumulation of Cr near it for most grain boundaries, thereby inhibiting the co-segregation of Cr and C, making it difficult for B, C, and Cr to aggregate at most grain boundaries. This is beneficial for controlling the nucleation of Cr₂₃(BC)₆.

Keywords: austenitic steel; boron; Cr₂₃(BC)₆; grain boundary segregation; first principles



Citation: Yan, X.; Xu, P.; Han, P.; Dong, N.; Wang, J.; Zhang, C. The Effect of B on the Co-Segregation of C-Cr at Grain Boundaries in Austenitic Steels. *Metals* **2023**, *13*, 1044. <https://doi.org/10.3390/met13061044>

Academic Editor: Pavel Lejček

Received: 20 April 2023

Revised: 29 May 2023

Accepted: 29 May 2023

Published: 30 May 2023



Copyright: © 2023 by the authors. Licensee MDPI, Basel, Switzerland. This article is an open access article distributed under the terms and conditions of the Creative Commons Attribution (CC BY) license (<https://creativecommons.org/licenses/by/4.0/>).

1. Introduction

Cr is widely used as an alloying element in stainless steels due to its ability to greatly enhance their corrosion resistance. This enhancement is primarily achieved through the formation of Cr₂O₃ passivation film on the surface of the steel. When Cr reacts with oxygen, it ends up forming this tightly bound protective layer. This passivation film acts as a barrier between the reactive metal and corrosive environment, helping to prevent further interactions [1]. However, the excessive concentration of Cr can negatively impact the stability of the austenitic structure due to Cr being a typical ferrite-forming element, thereby restricting the material's thermal stability and causing it to undergo structural transformations, leading to reduced strength and toughness. To stabilize the austenitic structure and improve the strength of steels, it is necessary to add austenite-stable elements to austenitic steels such as N, Mn, and Ni. Moreover, the presence of excessive amounts of Cr can be detrimental to the performance and durability of austenitic stainless steels. One of the adverse effects of high Cr levels is the precipitation of sigma-(σ) and chi (χ)-phase precipitates at grain boundaries (GBs) [2,3]. These precipitates can initiate corrosion or reduce the steel's toughness and ductility, leading to catastrophic failures under stress. Moreover, when Cr combines with C and N, it tends to form various types of precipitates such as Cr₂₃C₆, CrN, and Cr₂N [4,5]. The formation of these precipitates can lead to a reduction in corrosion resistance due to the generation of depletion zones near GBs where the Cr availability is decreased. This depletion zone leads to localized corrosion in these areas, which can significantly reduce the life of austenitic stainless steels.

Cr₂₃C₆ carbides are common precipitates in austenitic stainless steels, typically forming at original austenite GBs, lath bundle boundaries, lath boundaries, and sub-GBs. The

precipitation of Cr_{23}C_6 carbides along GBs not only causes the formation of a Cr-depletion zone near these precipitates but also reduces the mechanical properties of stainless steels, and leads to GB brittleness. This is particularly problematic in austenitic heat-resistant steels during long-term operation at high temperatures, where precipitates at GBs are a leading cause of material failure [6,7]. To improve the service life of austenitic heat-resistant steels, it is crucial to find ways to restrain the precipitation of Cr_{23}C_6 carbides or slow down their coarsening speed. B, often referred to as a “vitamin” in steels [8–11], has extremely low solubility with concentrations typically in the range of several tens of ppm. In steels, B primarily distributes at or near GBs. B can effectively reduce the coarsening rate of M_{23}C_6 carbides at austenite GBs by hindering the Ostwald ripening of the carbides [12–16], though its effect on Cr_{23}C_6 growth in grains has been shown to be minimal [12]. In 9Cr steels, the segregation of B at GBs during the austenitization process of the steels effectively suppressed the precipitation of Cr_{23}C_6 carbides during tempering at 600 °C and 790 °C [16].

GBs are planar interfaces that separate neighboring grains within the polycrystalline structure of stainless steels and other metals. These regions can exhibit thermodynamic instability, leading to local changes in composition, mechanical properties, and susceptibility to various types of corrosion. Fortunately, adding specific alloying elements to the material can provide a mechanism to mitigate GB instabilities and improve the local structure and chemical properties of the boundary regions [17,18]. However, the atomic-level mechanisms of B influencing the formation of Cr_{23}C_6 [19], that is, the co-segregation mechanisms of C and Cr at GBs, and the effect of B on the segregation remain unclear. In recent years, there has been increasing interest in understanding the mechanisms of GB segregation within metallic materials. Among the various theoretical approaches available for investigating these complex phenomena, first-principles methods based on density functional theory (DFT) have emerged as a powerful tool. This is due to their ability to accurately predict the electronic and structural properties of materials, including the interfacial energetics and chemical bonding at the atomic scale. As a result, DFT-based simulations have become a standard approach in the study of GB segregation and related phenomena. In fact, a recent comprehensive review noted that these methods have been the most helpful tool for investigating GB segregation in metallic systems. To address this issue, based on the GB structures in austenitic heat-resistant steels, three symmetrical inclined GB models ($\Sigma 5$, $\Sigma 9$ and $\Sigma 11$) in fcc-Fe were constructed using the first-principles method in this paper. The segregation and co-segregation tendencies of C, B, and Cr atoms at these GBs were examined, and the effect of B on C-Cr segregation in austenitic heat-resistant steels was analyzed. The results provide a theoretical explanation for the formation of Cr_{23}C_6 and $\text{Cr}_{23}(\text{CB})_6$ carbides and the inhibition of B on their maturation at austenite GBs.

2. Computational Methods and Structural Models

2.1. Computational Methods

All calculations in this study were carried out using the Materials Studio (MS) software package [20]. The exchange-correlation energy is treated using the generalized gradient approximation combined with the affix projection plane wave method [21]. The plane wave cut-off energy for all calculations is set to 400 eV. The Brillouin zone is divided using the Monkhorst–Pack k-point grid method. The structure is optimized using the conjugate gradient method, with fixed cell size and shape but free atom positions. The energy convergence criterion is set to 1.0×10^{-5} eV, while the force convergence criterion is less than 0.01 eV/Å for each atom. To verify the rationality of the parameters, the total energies of the fcc-Fe unit cell versus lattice constants are calculated. Figure 1 displays the correlation between the total energies of the cell and the lattice constants. The lattice constant of fcc-Fe with the lowest energy is 3.43 Å, which closely aligns with the previously reported results [22–24].

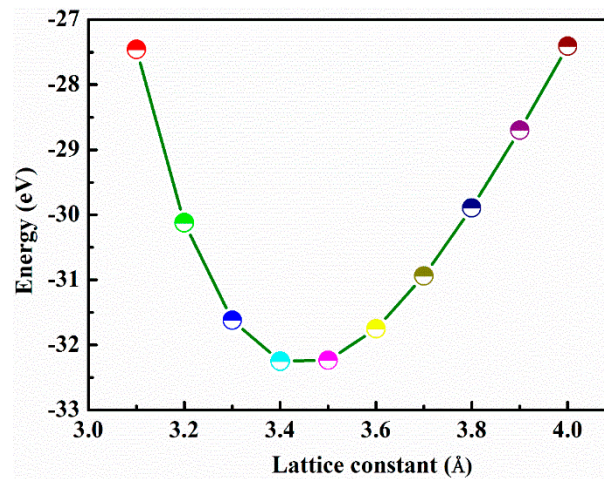


Figure 1. Total energies of fcc-Fe unit cell versus lattice constants.

Since the atomic radius of Cr is relatively large, the Cr atom is placed in the corresponding substitutional positions for the following calculation. In contrast, due to the smaller atomic radii, B and C atoms are located in the GB gap and octahedral interstitial space in other regions.

Taking the interstitial B atom as an example, the solution energy is [25]:

$$E_B^{sol} = E_{GB}^{Fe+B} - E_{GB}^{Fe} - E^B, \quad (1)$$

where E_{GB}^{Fe+B} represents the total energy of the GB supercell containing B, E_{GB}^{Fe} is the total energy of the GB supercell without B, and E^B represents the total energy of the B atom in vacuum (a cubic of $10 \text{ \AA} \times 10 \text{ \AA} \times 10 \text{ \AA}$). A negative or smaller value indicates that the B atom is more likely to occupy the corresponding site.

To investigate the segregation tendency of Cr, the segregation energy E_{seg}^{Cr} can be calculated using the following formulas [26,27]:

$$E_{seg}^{Cr} = E_{GB}^{Cr} - E_{block}^{Cr}, \quad (2)$$

where E_{GB}^{Cr} and E_{block}^{Cr} represent the impurity energies of Cr atom at the GB and in the block, respectively, which can be obtained from the following equations:

$$E_{GB}^{Cr} = E_{GB}^{(N-1)Fe+Cr} - E_{GB}^{Fe} - \mu_{Cr}, \quad (3)$$

$$E_{block}^{Cr} = E_{block}^{(N-1)Fe+Cr} - E_{block}^{Fe} - \mu_{Cr}, \quad (4)$$

here, $E_{GB/block}^{(N-1)Fe+Cr}$ is the total energy of the GB/block structure containing Cr atom, while E_{block}^{Fe} is the total energy of the block structure without Cr, and μ_{Cr} represents the chemical potential. Therefore, in combination with Equation (2), the segregation energy E_{seg}^{Cr} can be expressed as:

$$E_{seg}^{Cr} = \left(E_{GB}^{(N-1)Fe+Cr} - E_{GB}^{Fe} \right) - \left(E_{block}^{(N-1)Fe+Cr} - E_{block}^{Fe} \right). \quad (5)$$

The lower the E_{seg}^{Cr} value, the stronger the segregation tendency of Cr.

As interstitial microalloying elements, the formula for calculating the segregation energy of B and C differs slightly. Taking B as an example, the segregation energy can be calculated using the following formula:

$$E_{seg}^B = \left(E_{GB}^{Fe+B} - E_{GB}^{Fe} \right) - \left(E_{block}^{Fe+B} - E_{block}^{Fe} \right), \quad (6)$$

where $E_{GB/block}^{Fe+B}$ represents the total energy of the GB/block structure containing B atoms.

To further investigate the effect of B on the segregation of Cr at GBs, the most stable segregation site of B atoms at each GB is pre-filled with B atoms, and then the segregation energy of Cr is calculated using the following equation:

$$E_{seg}^{Cr+B} = \left(E_{GB}^{(N-1)Fe+Cr+B} - E_{GB}^{Fe+B} \right) - \left(E_{block}^{(N-1)Fe+Cr} - E_{block}^{Fe} \right), \quad (7)$$

where $E_{GB}^{(N-1)Fe+Cr+B}$ represents the total energy of the GB structure containing both Cr and pre-segregated B atoms.

If considering the interaction of interstitial atoms, such as B and C atoms, when they co-segregate at GBs, the co-segregation energy of the B-C pair can be expressed as follows:

$$E_{coseg}^{B+C} = \left(E_{GB}^{Fe+B+C} - E_{block}^{Fe+B} - E_{block}^{Fe+C} + 2E_{block}^{Fe} - E_{GB}^{Fe} \right) / 2, \quad (8)$$

here, $E_{GB/block}^{Fe+B+C}$ is the total energy of the GB/block structure containing both B and C atoms, and E_{block}^{Fe+C} represents the total energy of the block structure only containing C atom.

To determine the interaction between Cr and an interstitial atom, their interaction energy is introduced. The interaction energy between Cr and interstitial B atoms, denoted as E_i^{B+Cr} , can be expressed as follows:

$$E_i^{B+Cr} = \left(E_{GB}^{(N-1)Fe+Cr+B} + E_{GB}^{Fe} \right) - \left(E_{GB}^{(N-1)Fe+Cr} + E_{GB}^{Fe+B} \right). \quad (9)$$

The negative value of E_i^{B+Cr} indicates that B and Cr are attracting each other, while a positive value means a mutual exclusion.

2.2. Structural Models

Due to limited computational power, the GB structures for first-principles calculations typically select the interfaces with low GB energy, rather than the random GBs with a large number of atoms. Based on the experimental results of austenitic stainless steels [28] and relaxed fcc-Fe unit cells, the $\Sigma 5(210)$, $\Sigma 9(221)$ and $\Sigma 11(113)$ GBs were constructed in this study, and Figure 2 illustrates their schematic illustration. The crystal cells used for free surface calculations are of identical size to those used for GB models. Taking $\Sigma 5(210)[001]$ GB as an example, the process of constructing GB models is explained: use $[001]$ crystallographic direction as the rotation axis for the (210) crystal face of fcc-Fe, and splice the two crystals after rotating 53.13° . The splicing of two crystals results in the coincidence of the sublattice positions of the two lattices, thereby merging sites that are too close to each other [29].

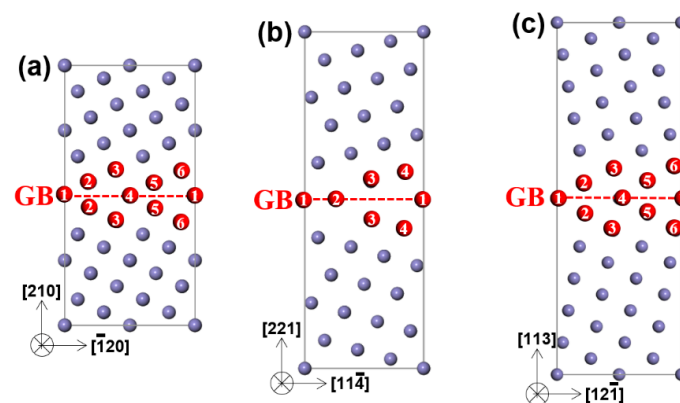


Figure 2. Schematic illustration of (a) $\Sigma 5(210)$, (b) $\Sigma 9(221)$ and (c) $\Sigma 11(113)$ GBs, respectively. The atomic sites for substitution are marked in red.

Alloy atoms may occupy any one of multiple sites at or near the GB during its segregation. Based on the symmetry of GBs, 6, 4, and 6 potential substitutional sites were selected for the $\Sigma 5(210)$, $\Sigma 9(221)$ and $\Sigma 11(113)$ GBs, respectively, and their specific locations are shown in Figure 2. Specifically, three groups of equivalence sites were selected for the $\Sigma 5(210)$ and $\Sigma 11(113)$ GBs, namely sites 1 and 4 on the GB interfaces, sites 2 and 5 closest to the GB interfaces, and sites 3 and 6. It should be noted that although every two sites are equivalent in position for the clean fcc-Fe, they are no longer equivalent when considering the influence of interstitial atoms due to the different distances from these atoms. Unlike these two GBs, four completely different sites in symmetry were selected for the $\Sigma 9(221)$ GB.

3. Results and Discussion

3.1. Segregation Tendencies of B, C, and Cr at GBs

The insets of Figure 3 provide the potential segregation sites of interstitial atoms at the three GBs, labeled as 1–5. According to the different polyhedral structures around these interstitial sites, they are classified into three types: tetrahedron (blue), pentahedron (yellow), and octahedron (red). Figure 3 compares the solution energies of B and C at these interstitial sites of the $\Sigma 5(210)$, $\Sigma 9(221)$ and $\Sigma 11(113)$ GBs, respectively, analyzing their occupancy tendencies at all sites. The solution energies of B and C atoms vary greatly depending on the interstitial sites. Since the atomic radius and number of extranuclear electrons of C is smaller than those of B, C has much lower solution energies, making it more prone to segregate to the interstitial sites at GBs. For the $\Sigma 5(210)$ GB, B and C have negative solution energy at interstitial sites 2–5, with the lowest energy at site 3 being the most stable segregation position. Similarly, the only most stable segregation position for B and C at the $\Sigma 9(221)$ GB is site 3; however, there are two most stable segregation positions, sites 3 and 4, for B and C at $\Sigma 11(113)$ GB.

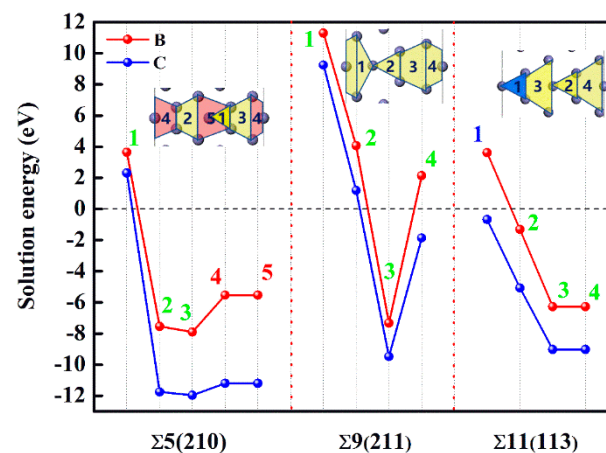


Figure 3. Solution energies of B and C at interstitial sites of the three GBs, respectively.

The segregation energies of B and C atoms at the stable interstitial sites of the three GBs depicted in Figure 3 were calculated. The results are presented in Figure 4, which shows that the segregation energies of B and C atoms at the $\Sigma 5(210)$, $\Sigma 9(221)$, and $\Sigma 11(113)$ GBs are -4.44 , -3.87 , -2.81 eV and -2.45 , -2.28 , -1.83 eV, respectively. Notably, the segregation energies of the B atom are significantly lower than those of the C atom, indicating that the three GBs have a stronger ability to capture B atoms. The $\Sigma 11(113)$ GB has a smaller GB energy and excess volume and a more compact structure [30]; therefore, in comparison with the $\Sigma 5(210)$ GB, the $\Sigma 11(113)$ GB has a weaker ability to capture B and C atoms, and the ability of the $\Sigma 9(221)$ GB is also relatively weaker. The strongest segregation tendency of B and C atoms is observed at $\Sigma 5(210)$ GB, and their second strongest segregation tendency is to the $\Sigma 9(221)$ GB.

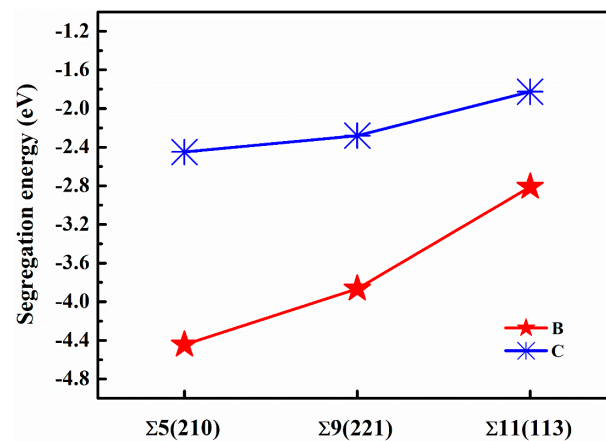


Figure 4. Segregation energies of B and C at their most stable interstitial sites of the three GBs.

Cr in steels has a tendency to form precipitated phases such as Cr_{23}C_6 at GBs with C, so the segregation energies of Cr at the potential substitutional sites in Figure 2 were calculated for the $\Sigma 5(210)$, $\Sigma 9(221)$, and $\Sigma 11(113)$ GBs. Figure 5 depicts the segregation tendencies of Cr at these substitutional sites. The segregation tendencies of Cr vary at different substitutional sites, and its segregation energies at all sites are negative with small absolute values, indicating its slight segregation tendency at all the three GBs. For $\Sigma 5(210)$ GB, due to the small atomic radius, Cr is more likely to segregate at sites 3 and 6, which have relatively smaller coordination numbers, average nearest neighbor distances, and corresponding polyhedron volumes. For the $\Sigma 9(221)$ and $\Sigma 11(113)$ GBs, which feature denser structures, Cr typically segregates to specific sites at the interfaces of the GBs. Specifically, it tends to segregate at sites 1 and 2 of the $\Sigma 9(221)$ GB and at sites 1 and 4 of the $\Sigma 11(113)$ GB.

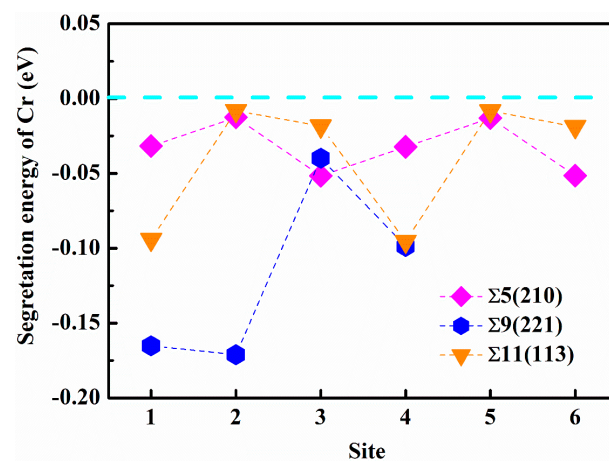


Figure 5. Segregation energies of Cr at substitutional sites of the three GBs, respectively.

3.2. Co-Segregation Tendencies of C-Cr, B-C, and B-Cr at GBs

The analysis presented above investigates the tendency of single alloy atoms, such as B, C, and Cr, to segregate at the $\Sigma 5(210)$, $\Sigma 9(221)$, and $\Sigma 11(113)$ GBs. The results indicate that B exhibits the strongest segregation tendency, followed by C. In comparison with single-element segregation, the co-segregation of multiple elements at GBs is more common, so it is necessary to study the co-segregation trends of multiple elements. In view of the easy formation for Cr_{23}C_6 in austenitic stainless steels, the co-segregation trend of Cr and C was analyzed firstly. After pre-placing C at its most stable interstitial segregation site because of its stronger segregation tendency, the segregation energies of Cr at the potential substitutional sites of the three GBs were calculated, which were named the co-segregation

energies of the C-Cr pair. Figure 6 reveals the co-segregation energies of the C-Cr pair at the $\Sigma 5(210)$, $\Sigma 9(221)$, and $\Sigma 11(113)$ GBs. The results indicate that the C-Cr pair is prone to co-segregate at the three GBs. The lowest co-segregation energy values of the C-Cr pair are -0.112 , -0.214 and -0.116 eV for the $\Sigma 5(210)$, $\Sigma 9(221)$, and $\Sigma 11(113)$ GBs, respectively. These values are all lower than the minimum segregation energy of a single Cr atom at the three GBs in Figure 4, which are -0.05 , -0.171 , and -0.095 eV, respectively. In addition, the bond lengths of the C-Cr pair with the lowest co-segregation energies at the $\Sigma 5(210)$, $\Sigma 9(221)$, and $\Sigma 11(113)$ GBs are 2.276, 3.773, and 3.506 Å, respectively, similar to the interatomic distance of C to Cr in Cr_{23}C_6 . These results suggest that the C-Cr pair is more likely to co-segregate at GBs, thereby creating favorable conditions for the formation of Cr and C complexes.

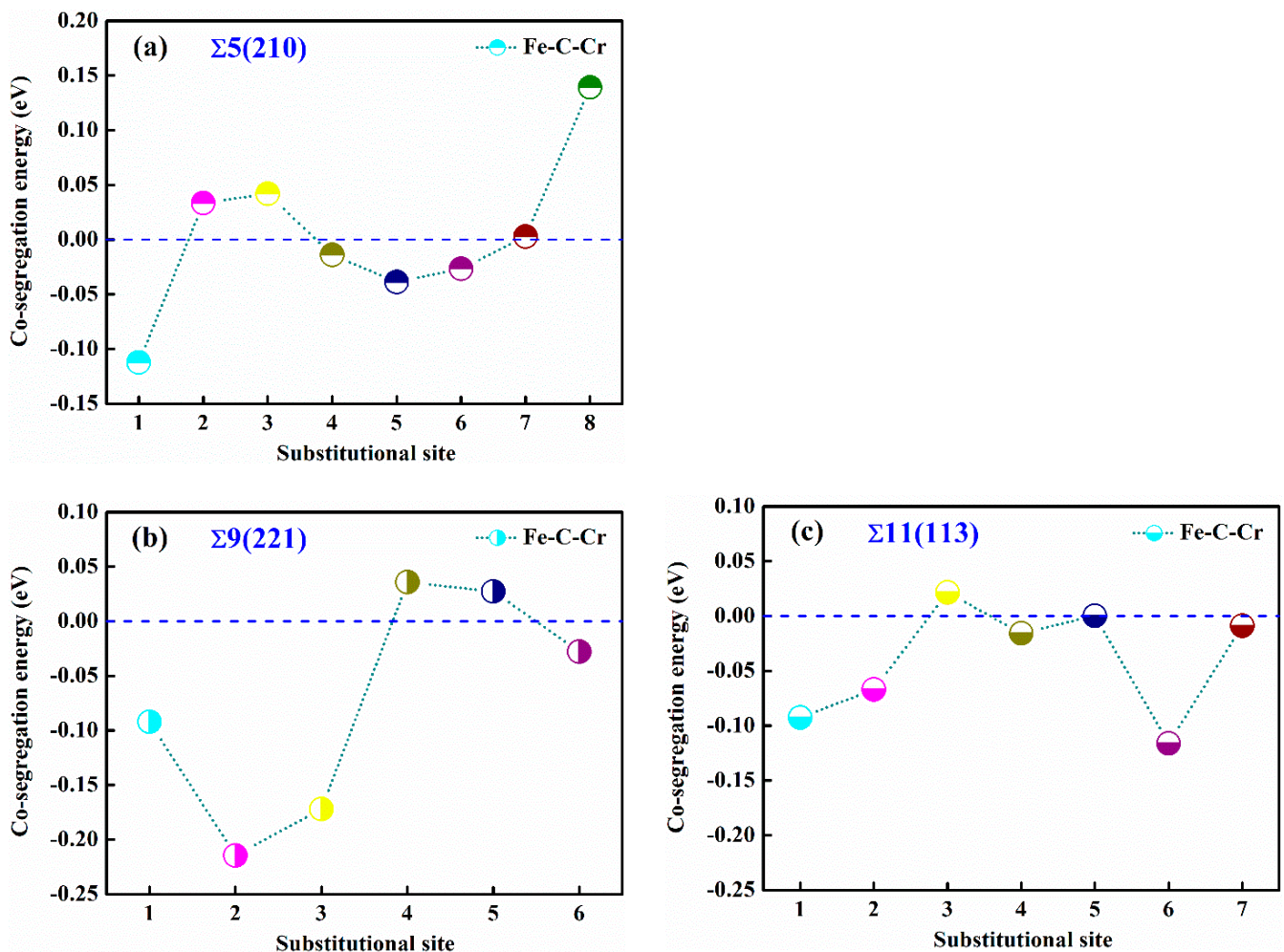


Figure 6. Co-segregation energies of C-Cr pair when Cr at substitutional sites of the three GBs, respectively. C atom was pre-placed at its most stable interstitial segregation site.

The influence of grain boundary B on the segregation tendencies of C at the $\Sigma 5(210)$, $\Sigma 9(221)$, and $\Sigma 11(113)$ GBs was also analyzed. To simplify the representation, interstitial sites at GBs were denoted as N-a/b after symmetry. Taking the $\Sigma 5(210)$ GB as an example, the interstitial site 3 was subdivided into site 3-a and site 3-b, and the site 3-a was pre-occupied by B because of the lowest segregation energy for B at site 3 according to the results of Figures 3 and 4. Subsequently, based on the pre-segregation of B, the B-C co-segregation energies were calculated for C occupying another interstitial site (1, 2, 3-b, 4-a, 4-b, or 5) at the $\Sigma 5(210)$ GB. Figure 7 describes the co-segregation energies of B-C pair at the three GBs. The co-segregation energy of B-C pair at site 3-b of $\Sigma 5(210)$ GB is the lowest,

indicating that the B-C pair has a tendency to co-segregate at the sites 3-a and 3-b, as shown in the local structure schematic of Figure 7. Additionally, the optimal co-segregation sites of the B-C pair at the $\Sigma 9(221)$ and $\Sigma 11(113)$ GBs are identified as the sites 3-a and 3-b and the sites 4-a and 3. As B is pre-occupying the most stable interstitial site, the co-segregation energy of the B-C pair is lower than a single B atom regardless of the position of C, which indicates that the B segregation at GBs promotes the grain boundary segregation of C. C tends to fill at the most or second most stable interstitial segregation site of the three GBs, even if B has been pre-segregated at the most stable interstitial segregation site. The reason may be that the B segregation can cause local structural distortion at the three GBs, which promotes the segregation of C. Specifically, when B was pre-placed at its most stable interstitial segregation site of the $\Sigma 5(210)$ and $\Sigma 9(221)$ GBs, C would co-segregate to another interstitial site that has the same symmetry as the segregation site where B occupied. When B pre-segregated at its most stable interstitial segregation site of the $\Sigma 11(113)$ GB, C would co-segregate to the most stable interstitial segregation site with a similar segregation tendency. Consequently, the pre-segregation of B mostly affects the segregation tendency of the B-C pair and has little influence on their segregation position.

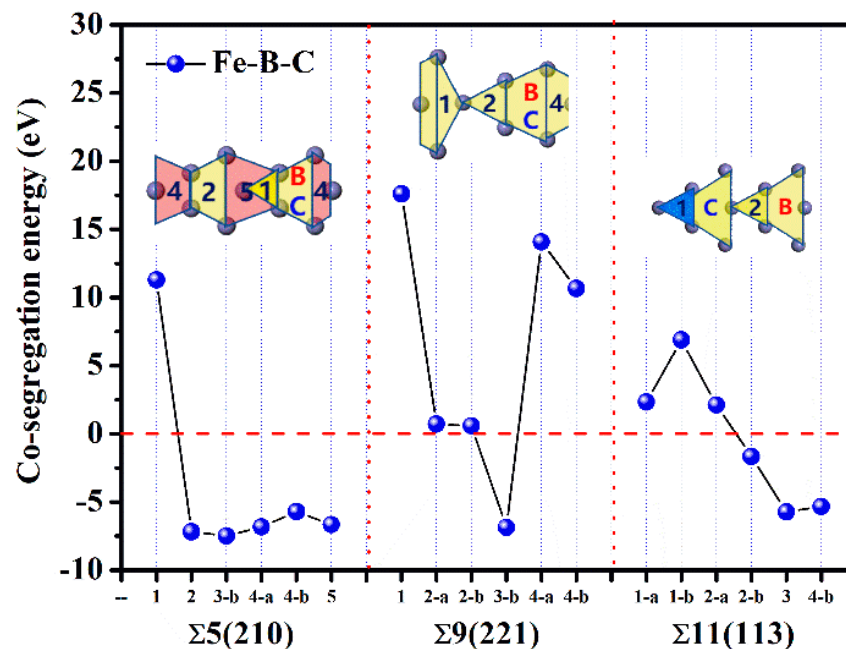


Figure 7. Co-segregation energies of B-C pair at the three GBs, respectively.

Figure 8 demonstrates the relationship between co-segregation energies of the B-C pair and the interatomic distance of the B and C atoms when they co-segregate at the $\Sigma 5(210)$, $\Sigma 9(221)$, and $\Sigma 11(113)$ GBs. Except for the $\Sigma 11(113)$ GB, the co-segregation energies of the B-C pair decreases as the interatomic distance of the B and C atoms increases. This phenomenon occurs because the larger the distance of B and C atoms, the smaller the repulsion between them and the stronger the co-segregation tendency for them. When co-segregation occurs at the $\Sigma 11(113)$ GB, the repulsion can be ignored due to the large distance of B and C atoms of above 4 Å; however, the corresponding co-segregation energy remains too high, which should be related to the special structure of the GB and the characteristics of interstitial sites.

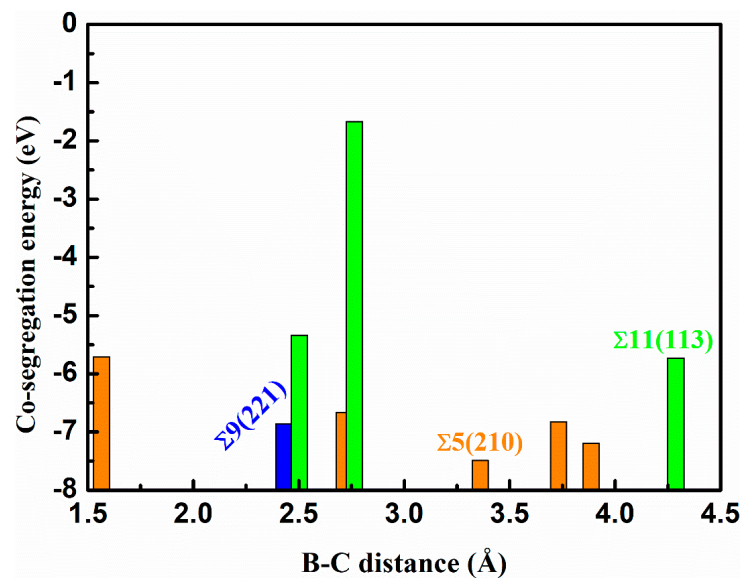


Figure 8. Relationship between co-segregation energies of B-C pair and their interatomic distances at the three GBs.

As interstitial atoms, B and C are highly susceptible to segregation at GBs, with a significant interaction between them and Cr atoms at or near GBs. To better investigate the co-segregation tendency and distribution at GBs of the main elements in Cr_{23}C_6 and $\text{Cr}_{23}(\text{BC})_6$, B, C, and Cr, Figure 9 shows the interaction energies between the grain boundary B (or C) atom and Cr atom at or near the $\Sigma 5(210)$, $\Sigma 9(221)$, and $\Sigma 11(113)$ GBs. The interaction energy values between the C and Cr atoms at the three GBs are all less than -1.0 eV, which are significantly lower than those of the B-Cr pair. This suggests that the grain boundary C atom has a strong attraction to the Cr atom, creating conditions for the nucleation of Cr_{23}C_6 carbides. Unlike the C atom, the grain boundary B has only a slight attraction to most Cr atoms at or near the $\Sigma 5(210)$ GB, except for the Cr atom at site 3. While B has a negligible effect on most Cr atoms at or near the $\Sigma 9(221)$ GB, except for the Cr atom at site 6 with a visible repulsive effect. At the $\Sigma 11(113)$ GB, B exhibits a significant repulsive effect on the Cr atom at sites 3 and 4, while the interaction with other Cr atoms is approximately zero. In summary, in the absence of B at GBs, the interstitial segregation of C atom at GBs will attract Cr atom from the matrix towards GBs, promoting nucleation of Cr_{23}C_6 . When B exists near GBs, it will occupy the most stable interstitial segregation site firstly due to its stronger segregation tendency. Considering that interstitial C atoms still segregate to GBs, it is possible to create conditions for nucleation of $\text{Cr}_{23}(\text{BC})_6$, especially for the $\Sigma 5(210)$ GB. The B atom at the $\Sigma 9(221)$ and $\Sigma 11(113)$ GBs has a certain inhibitory effect on the Cr segregation, while C atoms can continue to segregate towards GBs, accumulating some Cr atoms nearby. Overall, in comparison with the GBs without B, the pre-co-segregation of B and C atoms at GBs decreases the co-segregation tendency of Cr to the GBs.

In austenitic stainless steels, B can suppress the precipitation of precipitates, reducing their amount at GBs. Existing experimental results show that B atoms easily segregate to GBs, transforming Cr_{23}C_6 into $\text{Cr}_{23}(\text{CB})_6$. To further analyze the formation mechanism of $\text{Cr}_{23}(\text{CB})_6$, Figure 10 delineates the segregation energies of Cr at any substitutional site of the three GBs, the co-segregation energies of C-Cr pair when C is fixed to its most stable interstitial site, and the co-segregation energies of B-C-Cr when C and B are anchored to their most stable interstitial sites, which were taken to analyze the segregation behavior of Cr and C-Cr at the three GBs, as well as the role of B. The alloy element Cr has different degrees of segregation tendency at all the three GBs, and it is more likely to segregate at the $\Sigma 9(221)$ GB, while its segregation tendencies are weaker at the $\Sigma 5(210)$ and $\Sigma 11(113)$ GBs. The co-segregation energies of the C-Cr pair at the three GBs are significantly lower than those of single Cr atom, indicating that interstitial C atom can promote Cr segregation

to GBs. C-Cr is prone to co-segregate at GBs, and the resulting C-Cr aggregates provide a conducive environment for the nucleation of Cr-C compounds. B shows different effects on the co-segregation of the C-Cr pair at the $\Sigma 5$, $\Sigma 9$ and $\Sigma 11$ GBs. B promotes the segregation of C-Cr at the $\Sigma 5(210)$ GB and has little effect at the $\Sigma 9(221)$ GB while exhibiting a significant inhibitory effect at the $\Sigma 11(113)$ GB.

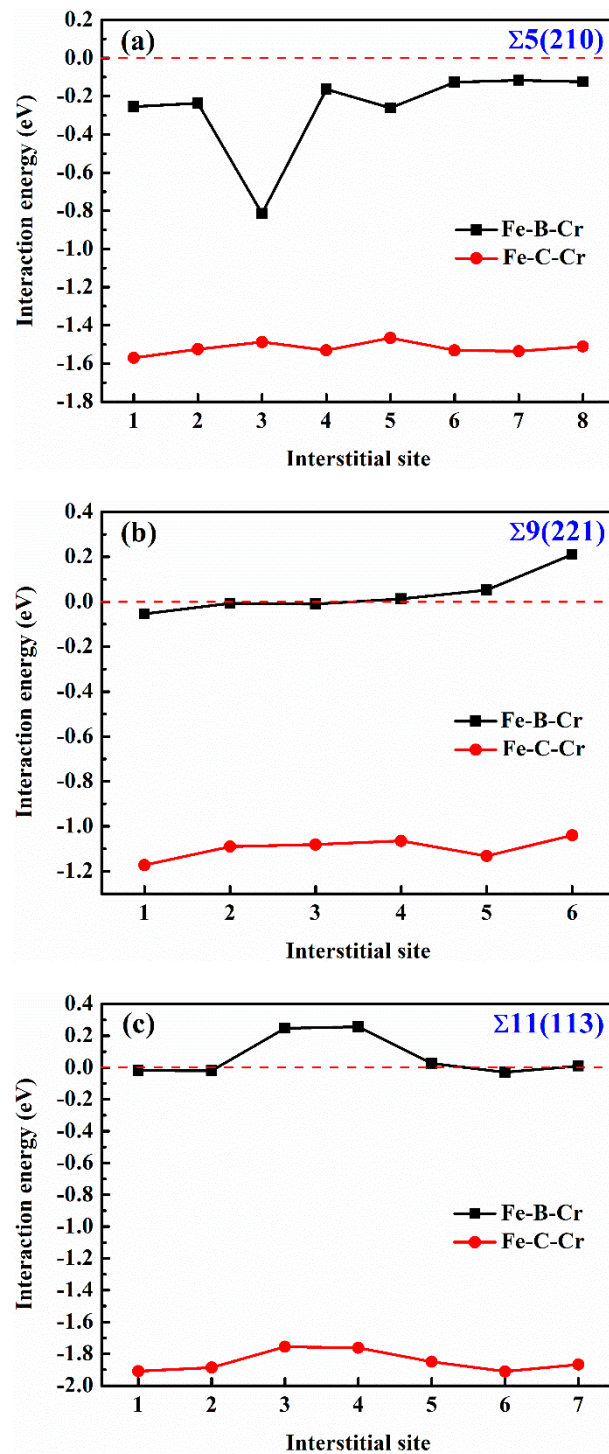


Figure 9. Interaction energies of B-Cr and C-Cr when Cr at substitutional sites of the three GBs, respectively. B and C atoms were pre-placed at their most stable interstitial sites. (a) $\Sigma 5(210)$; (b) $\Sigma 9(221)$; (c) $\Sigma 11(113)$.

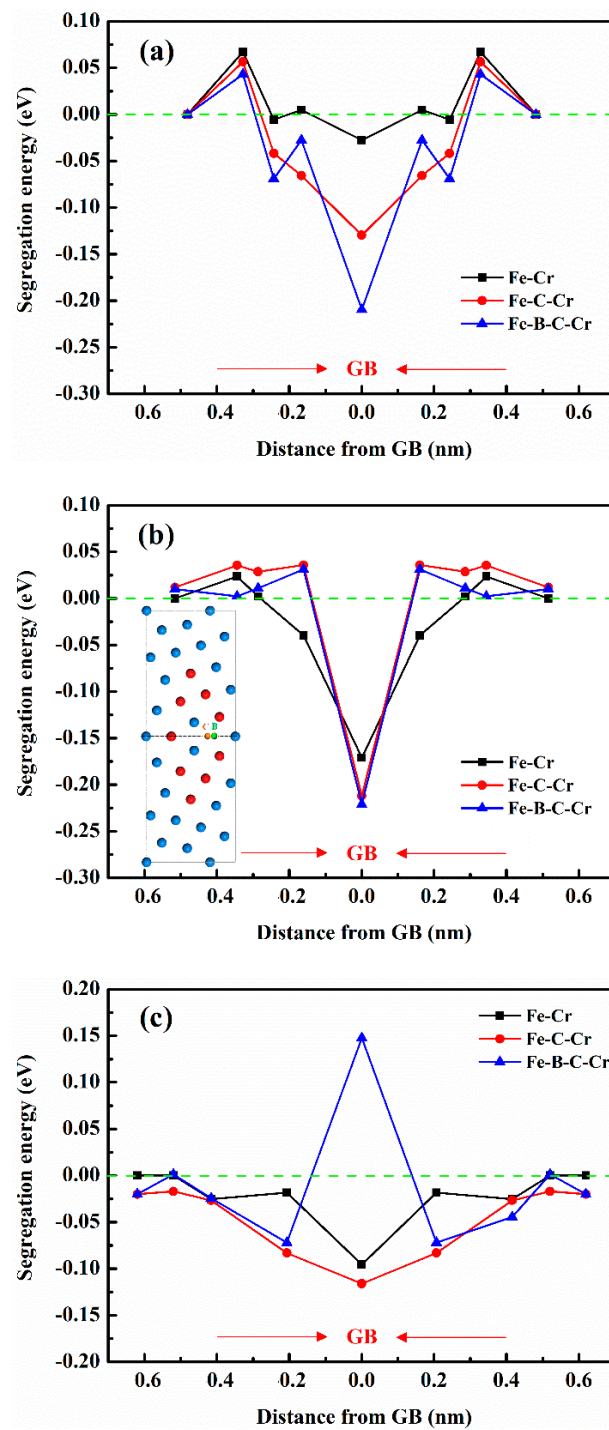


Figure 10. Segregation energies versus the distance from GB plane for Cr, C-Cr, and B-C-Cr at (a) $\Sigma 5(210)$, (b) $\Sigma 9(221)$, and (c) $\Sigma 11(113)$ GBs, respectively.

4. Conclusions

Density functional theory was employed to investigate the segregation and co-segregation tendencies of B, C, and Cr at the low-energy GBs of $\Sigma 5(210)$, $\Sigma 9(221)$, and $\Sigma 11(113)$ in austenitic steels and analyze the micro-mechanism of their co-segregation, leading to the following conclusions:

- (1) B, C, and Cr all tend to segregate at the $\Sigma 5(210)$, $\Sigma 9(221)$, and $\Sigma 11(113)$ GBs. B and C are more prone to segregate at GBs than Cr, especially at the $\Sigma 5(210)$ GB.

- (2) C and Cr tend to co-segregate at the $\Sigma 5(210)$, $\Sigma 9(221)$, and $\Sigma 11(113)$ GBs with short interatomic distances, and their segregation region is much wider for the $\Sigma 9(221)$ GB. B and C easily co-segregate at the three GBs, but their interatomic distances are far apart. Grain boundary B has a certain inhibitory effect on Cr segregation in its vicinity, especially at the $\Sigma 9(221)$ and $\Sigma 11(113)$ GBs.
- (3) When B exists at the $\Sigma 5(210)$ GB, B, C, and Cr tend to co-segregate at the GB, while if B was pre-placed at the $\Sigma 9(221)$ and $\Sigma 11(113)$ GBs, it exhibits a certain inhibitory effect on the Cr segregation at the two GBs.

Author Contributions: Conceptualization, P.X. and P.H.; Formal analysis, X.Y.; Funding acquisition, P.H.; Investigation, X.Y., N.D., J.W. and C.Z.; Methodology, P.X., N.D., J.W. and C.Z.; Resources, N.D. and J.W.; Software, C.Z.; Visualization, X.Y.; Writing—original draft, X.Y.; Writing—review and editing, P.X. and P.H. All authors have read and agreed to the published version of the manuscript.

Funding: The present work was financially supported by National Natural Science Foundation of China (Grant No. 51871159).

Data Availability Statement: The data that support the findings of this study are available from the corresponding author upon reasonable request.

Acknowledgments: We would like to express our sincere gratitude to Jin Chen for his valuable guidance in revising this paper.

Conflicts of Interest: The authors declare that they have no conflict of interest.

References

1. Zhang, W.H. *Stainless Steels and the Heat Treatment*, 1st ed.; Liaoning Science and Technology Press: Shenyang, China, 2010; pp. 23–25.
2. Menzel, J.; Kirschner, W.; Stein, G. High nitrogen containing Ni-free austenitic steels for medical applications. *ISIJ Int.* **1996**, *36*, 893–900. [[CrossRef](#)]
3. Kim, S.J.; Lee, T.H. Precipitation sequences in austenitic Fe-22Cr-21Ni-6Mo-(N) stainless steels. *Mater. Sci. Forum* **1999**, *318*, 109–114. [[CrossRef](#)]
4. Simmons, J.W.; Covino, B.S., Jr.; Hawk, J.A.; Dunning, J.S. Effect of nitride (Cr_2N) precipitation on the mechanical, corrosion, and wear properties of austenitic stainless steel. *ISIJ Int.* **1996**, *36*, 846–854. [[CrossRef](#)]
5. Ha, H.Y.; Kwon, H.S. Effects of Cr_2N on the pitting corrosion of high nitrogen stainless steels. *Electrochim. Acta* **2007**, *52*, 2175–2180. [[CrossRef](#)]
6. Liu, G.; Han, Y.; Shi, Z.; Sun, J.; Zou, D.; Qiao, G. Hot deformation and optimization of process parameters of an as-cast 6Mo superaustenitic stainless steel: A study with processing map. *Mater. Des.* **2014**, *53*, 662–672. [[CrossRef](#)]
7. Pu, E.; Zheng, W.; Xiang, J.; Song, Z.; Feng, H.; Zhu, Y. Hot working characteristic of superaustenitic stainless steel 254SMO. *Acta Metall. Sin.* **2014**, *27*, 313–323. [[CrossRef](#)]
8. Wang, J.; Cui, Y.; Bai, J.; Dong, N.; Liu, Y.; Zhang, C.; Han, P. Effect of B addition on the microstructure and corrosion resistance of S31254 super austenitic stainless steels after solid solution treatment. *Mater. Lett.* **2019**, *252*, 60–63. [[CrossRef](#)]
9. Wang, J.; Cui, Y.; Bai, J.; Dong, N.; Liu, Y.; Zhang, C.; Han, P. The mechanism on the B addition to regulate phase precipitation and improve intergranular corrosion resistance in UNS S31254 superaustenitic stainless steels. *J. Electrochem. Soc.* **2019**, *166*, 600–608. [[CrossRef](#)]
10. Yu, J.; Zhang, S.; Li, H.; Jiang, Z.; Feng, H.; Xu, P.; Han, P. Influence mechanism of boron segregation on the microstructure evolution and hot ductility of super austenitic stainless steel S32654. *J. Mater. Sci. Technol.* **2022**, *112*, 184–194. [[CrossRef](#)]
11. Wu, M.W.; Lin, Z.J.; Lin, C.Y.; Chi, S.X.; Tsai, M.K.; Ni, K. Mechanical properties and fracture mechanism of boron-containing 304L austenitic stainless steel densified by liquid phase sintering. *Mater. Sci. Eng. A* **2021**, *814*, 141182. [[CrossRef](#)]
12. Abe, F. Research and development of heat-resistant materials for advanced USC power plants with steam temperatures of 700 °C and above. *Engineering* **2015**, *1*, 211–224. [[CrossRef](#)]
13. Abe, F. Behavior of boron in 9Cr heat resistant steel during heat treatment and creep deformation. *Key Eng. Mater.* **2007**, *345*, 569–572. [[CrossRef](#)]
14. Golpayegani, A.; Liu, F.; Svensson, H.; Andersson, M.; Andrén, H.O. Microstructure of a creep-resistant 10 pct chromium steel containing 250 ppm boron. *Metall. Mater. Trans. A* **2011**, *42*, 940–951. [[CrossRef](#)]
15. Hättestrand, M.; Andrén, H.-O. Boron distribution in 9–12% chromium steels. *Mater. Sci. Eng. A* **1999**, *270*, 33–37. [[CrossRef](#)]
16. Osanai, T.; Sekido, N.; Yonemura, M.; Maruyama, K.; Takeuchi, M.; Yoshimi, K. Evolution of boron segregation during tempering in B doped 9%Cr ferritic steel. *Mater. Charact.* **2021**, *177*, 111192. [[CrossRef](#)]
17. Wang, Q.; Wang, L.; Zhang, W.; Li, J.; Chou, K. Effect of cerium on the austenitic nucleation and growth of high-Mo austenitic stainless steel. *Metall. Mater. Trans. B* **2020**, *51*, 1773–1783. [[CrossRef](#)]

18. Wang, Q.; Wang, L.; Sun, Y.; Zhao, A.; Zhang, W.; Li, J.; Dong, H.; Chou, K. The influence of Ce micro-alloying on the precipitation of intermetallic sigma phase during solidification of super-austenitic stainless steels. *J. Alloys Compd.* **2020**, *815*, 152418. [[CrossRef](#)]
19. Suikkanen, P. Development and Processing of Low Carbon Bainitic Steels. Ph.D. Thesis, University of Oulu, Oulu, Finland, 2009.
20. Segall, M.D.; Lindan, P.J.D.; Probert, M.J.; Pickard, C.J.; Hasnip, P.J.; Clark, S.J.; Payne, M.C. First-principles simulation: Ideas, illustrations and the CASTEP code. *J. Phys.-Condens. Mat.* **2002**, *14*, 2717–2744. [[CrossRef](#)]
21. Basinski, Z.S.; Hume-Rothery, W.; Sutton, A.L. The lattice expansion of iron. *Proc. R. Soc. Lond. A Math. Phys. Sci.* **1955**, *229*, 459–467. [[CrossRef](#)]
22. Shang, J.X.; Wang, C.Y. Electronic effects of alloying elements Nb and V on body-centred-cubic Fe grain boundary cohesion. *J. Phys.-Condens. Mat.* **2001**, *13*, 9635–9644. [[CrossRef](#)]
23. Tran, R.; Xu, Z.; Zhou, N.; Radhakrishnan, B.; Luo, J.; Ong, S.P. Computational study of metallic dopant segregation and embrittlement at molybdenum grain boundaries. *Acta Mater.* **2016**, *117*, 91–99. [[CrossRef](#)]
24. Bean, J.J.; McKenna, K.P. Origin of differences in the excess volume of copper and nickel grain boundaries. *Acta Mater.* **2016**, *110*, 246–257. [[CrossRef](#)]
25. Yang, Y.; Ding, J.; Zhang, P.; Mei, X.; Huang, S.; Zhao, J. The effect of Cr on He segregation and diffusion at $\Sigma 3$ (112) grain boundary in α -Fe. *Nucl. Instrum. Methods Phys. Res. B Beam Interact. Mater. At.* **2019**, *456*, 7–11. [[CrossRef](#)]
26. Lejcek, P. *Grain Boundary Segregation in Metals*, 1st ed.; Springer: Berlin/Heidelberg, Germany, 2010; pp. 38–50.
27. Zhao, D.; Løvvik, O.M.; Marthinsen, K.; Li, Y. Segregation of Mg, Cu and their effects on the strength of Al $\Sigma 5(210)[001]$ symmetrical tilt grain boundary. *Acta Mater.* **2018**, *145*, 235–246. [[CrossRef](#)]
28. Xu, P.P.; Ma, J.Y.; Jiang, Z.H.; Zhang, Y.; Liang, C.X.; Dong, N.; Han, P.D. Effects of B segregation on Mo-rich phase precipitation in S31254 super-austenitic stainless steels: Experimental and first-principles study. *Chin. Phys. B* **2022**, *31*, 116402. [[CrossRef](#)]
29. Zheng, H.; Li, X.G.; Tran, R.; Chen, C.; Horton, M.; Winston, D.; Persson, K.A.; Ong, S.P. Grain boundary properties of elemental metals. *Acta Mater.* **2020**, *186*, 40–49. [[CrossRef](#)]
30. Xu, P.P.; Han, P.D.; Zhang, Z.X.; Zhang, C.L.; Dong, N.; Wang, J. First-principles study of boron segregation in fcc-Fe grain boundaries and its influence on interface adhesive strength. *Acta Phys. Sin.-Chin. Ed.* **2021**, *70*, 166401. [[CrossRef](#)]

Disclaimer/Publisher's Note: The statements, opinions and data contained in all publications are solely those of the individual author(s) and contributor(s) and not of MDPI and/or the editor(s). MDPI and/or the editor(s) disclaim responsibility for any injury to people or property resulting from any ideas, methods, instructions or products referred to in the content.